Journal of Alloys and Compounds 897 (2022) 163124

Contents lists available at ScienceDirect

Journal of Alloys and Compounds

journal homepage: www.elsevier.com/locate/jalcom

Increased photocatalytic activity and selectivity towards methane of trimetallic NiTiAl-LDH

Manuel Molina-Muriel[a], Yong Peng[a], Hermenegildo García[a], Antonio Ribera[b,*]

[a] Instituto Universitario de Tecnología Química, Universitat Politécnica de València-Consejo Superior de Investigaciones Científicas, 46022 Valencia, Spain
[b] Instituto de Ciencia Molecular, Universitat de València, 46980 Paterna, Spain

ARTICLE INFO

Article history:
Received 1 September 2021
Received in revised form 1 December 2021
Accepted 2 December 2021
Available online 4 December 2021

Keywords:
Solar light photocatalysis, Solar energy conversion, CO_2 photoreduction
Layered double hydroxides
Methane
Selectivity
Ti-based layered double hydroxides

ABSTRACT

Layered double hydroxides is a rising family of materials with interesting photocatalytic properties that are starting to be employed on the CO_2 photoreduction to useful chemicals. However, the selectivity control towards high energy value products, such as methane or methanol, is one of the main issues of this process due to the easier formation of CO, which requires fewer electrons to be transferred, and the competition of hydrogen evolution reaction. In this work, a new LDH material containing Ni, Ti and Al within the structure was synthesised with the purpose of increasing the selectivity towards methane production. The material was tested under solar simulator conditions, yielding a methane production of 148 μmol g^{-1} h^{-1}, with a selectivity of 86%, one of the highest values reported for this kind of material, while the competition from hydrogen evolution was almost suppressed. The role of Ti directing the selectivity towards methane was confirmed, since no CH_4 was produced when NiAl-LDH catalyst was used instead.

1. Introduction

Decreasing the emissions of CO_2 to the atmosphere is one of the most urgent challenges that society faces nowadays [1,2]. One of the best ways to deal with this problem is the conversion of CO_2 into valuable carbon compounds such as CO, CH_4, CH_3OH and others, since CO_2 utilisation solves the environmental problem, while providing chemicals and fuels. Of all approaches that have been developed to transform CO_2, CO_2 photoreduction (CO_2PR) is among the most promising ones, allowing to produce valuable chemicals using sunlight as the primary energy source in a clean way [3–5].

Though a tangible progress has been achieved in this field in the recent years, still several issues need to be solved [6]. For example, most of the suitable photocatalysts for this reaction work under UV irradiation, whereas photocatalysts exhibit low efficiency upon solar light exposure. Fast recombination of the photogenerated charge carriers is also another major limitation of the CO_2PR efficiency. The control of the selectivity of the products evolved and the competition of H_2 evolution (a process thermodynamically and kinetically less demanding) is another important aspect to be considered [7]. All the above issues lead to the need of developing new materials than can improve the efficiency and selectivity of CO_2PR.

Layered double hydroxides (LDH) are a family of 2D layered materials known for their use as visible-light driven photocatalysts [8–12]. Their composition can be expressed by the general formula $[M^{II}_{1-x}M^{III}_{x}(OH)_2]^{x+}(A^{n-})_{x/n}{\cdot}mH_2O$, were M^{II} and M^{III} are divalent and trivalent metal cations and A is an anion that is located between the positively charged layers [13]. The cations are homogeneously distributed within the sheets. It is also possible to fit monovalent or tetravalent cations inside LDH, the only limitation being the ionic radius. Some advantages of LDHs, such as good activity, tuneable composition and properties, low cost, and low environmental impact have boosted the use of these materials as photocatalysts for CO_2PR in the recent years [9,14–18]. In addition, the surface hydroxyl groups act as a binding site for the acidic CO_2 molecule, improving the CO_2 adsorption [19].

Several attempts have been made to control the selectivity of the CO_2 reduction, eliminating the competition from H_2 evolution reaction (HER), and increasing the selectivity towards products like CH_3OH or CH_4, which need a suite of electrons and protons to be formed [1,20–24]. It is known that Ni-containing photocatalysts have an improved selectivity towards methane production [25–27]. The introduction of Ni in LDH structures, combined with the selection of the incident light wavelength (over 600 nm) has been reported to enhance the methane production while almost suppressing the evolution of H_2 [28–32]. Other studies have revealed that Ti-containing LDHs also have an increased selectivity towards methane production [33]. It could be thought that combining those two

* Corresponding author.
E-mail address: antonio.ribera@uv.es (A. Ribera).

https://doi.org/10.1016/j.jallcom.2021.163124
0925-8388/

elements (Ti and Ni) within the same material could result in an improvement of methane production versus other competing products, particularly carbon monoxide or hydrogen.

Herein, in this work a new trimetallic LDH material containing nickel, titanium and aluminium cations was prepared. Both the use of methanol as solvent and the addition of titanium to the synthesis direct the nucleation process, constructing a morphology where cross-linked nanolayers assemble in radial direction to form a nanoball 3D superstructure. This catalyst can reach 86% selectivity towards methane production by CO_2PR under solar light irradiation, overcoming the need to cut wavelengths under 600 nm to reach CH_4 selectivity. This research demonstrates the versatility of LDH materials, making possible to pre-design and select the optimal morphology and composition of the photocatalyst to increase the selectivity towards the target product.

2. Material and methods

2.1. Materials

$Ni(NO_3)_2{\cdot}6H_2O$, and triethanolamine (TEOA) were purchased from Alfa Aesar. $Al(NO_3)_3{\cdot}9H_2O$, $NiCl_2{\cdot}6H_2O$, $AlCl_3{\cdot}6H_2O$, Ti(IV) bis (ammonium lactate) dihydroxide, $LiClO_4$ and 5 wt% perfluorinated Nafion® resin solution were obtained from Sigma-Aldrich. Urea (99%) was purchased from Honeywell. Water used in all the experiments was milliQ purity grade.

2.2. Sample preparation

NiTiAl-LDH material was prepared by a modified solvothermal method described in the literature [34]. In brief, 0.30 g (1 mmol) of $Ni(NO_3)_2{\cdot}6H_2O$, 0.05 g (0.125 mmol) of $Al(NO_3)_3{\cdot}9H_2O$, 60 µL (0.125 mmol) of a 50 wt% aqueous solution of Ti(IV) bis(ammonium lactate) dihydroxide, and 0.12 g (2 mmol) of urea were dissolved in 40 ml of methanol. The mix was stirred for 15 min and then transferred to a 100 ml stainless steel autoclave and heated at 120 °C for 24 h. The light green solid was collected by vacuum filtration on a Büchner, washed with methanol and dried at room temperature in a desiccator with vacuum. For comparison, NiAl-LDH material was prepared following the same method, adding 0.10 g (0.25 mmol) of $Al(NO_3)_3{\cdot}9H_2O$ and no titanium precursor.

To study the effect of the morphology on the catalytic activity, NiTiAl-bulk was prepared following a hydrothermal procedure. In brief, 1.62 g (6.67 mmol) of $NiCl_2{\cdot}6H_2O$, 0.20 g (0.83 mmol) of $AlCl_3{\cdot}6H_2O$ and 400 µL (0.83 mmol) of a 50% wt. aqueous solution of Ti(IV) bis(ammonium lactate) dihydroxide were dissolved in 10 ml of water. After that, the pH was slowly increased to 9 by dropwise addition of a 2 M NaOH solution. Water was added until a total volume of 33 ml was achieved. Then, the mixture was transferred to a 45 ml stainless steel autoclave and heated at 105 °C for 48 h. The green solid was collected by vacuum filtration, washed with water, and dried at room temperature in a desiccator with vacuum.

2.3. Materials characterisation

Powder X-ray diffraction (PXRD) patterns were recorded on a Philips X'PERT diffractometer equipped with a graphite monochromator (40 kV and 45 mA) using the Cu Kα radiation (λ = 1.54178 Å) in the range 2θ = 5–90°. Field emission scanning electron microscopy (FESEM) images and energy dispersive X-ray (EDX) data were collected on a Zeiss Ultra 55 apparatus equipped with an EDX detector. Transmission electron microscopy (TEM) images were obtained on a JEOL JEM 2100 F apparatus. Diffuse reflectance UV–visible spectroscopy (DRS) spectra were recorder on a PerkinElmer Lambda 1050 spectrophotometer, with the sample supported on a Harrick Praying Mantis™ diffuse reflectance accessory. Dynamic light scattering (DLS) measurements were carried out on a Malvern Zetasizer Ultra equipment, using ethanol as solvent, with a concentration of catalyst of 0.075 g/L. Specific surface area of the materials was measured by N_2 adsorption isotherms at 77.3 K, using a Micromeritics ASAP 2010 instrument. XPS measurements were carried out on SPECS spectrometer equipped with a Phoibos 150 9MCD detector using a nonmonochromatic X-ray source (Al and Mg) operating a 200 W. XPS was calibrated against C 1s at 284.5 eV. CO adsorption experiments were performed on a Quantachrome Autosorb-1C equipment. First, samples were heated at 100 °C to eliminate adsorbed water on the surface of the materials. Then, they were degassed at 1333 Pa for 2 h and cooled down to 30 °C. Afterwards, pure CO was introduced for the measurement of the adsorption isotherm (i. e. the total CO uptake).

Electrochemical impedance spectroscopy (EIS) and photocurrent measurements were performed using a Princeton Applied Research VersaSTAT 3 potentiostat with a standard three-electrode single compartment quartz cell. EIS measurements were recorded using a 0.1 M Na_2SO_4 aqueous solution as the electrolyte. The scanning frequency range was 0.01 Hz–100 kHz at 0.625 V vs Ag/AgCl reference electrode. Photocurrent measurements were obtained in a 0.1 M $LiClO_4$ aqueous solution with a 5% (vol.) of methanol. The light source was a 300 W Xenon lamp, with and without a 380 nm cut-off filter. The working electrode was prepared by drop casting 80 µL of catalyst dispersion (10 mg of catalyst, 170 µL of ethanol and 47 µL of a commercial perfluorinated Nafion® resin solution, 5 wt%) onto a FTO glass electrode. The area covered by the catalyst dispersion was 0.7 cm^2 (0.7 × 1 cm). Pt and Ag/AgCl electrodes were used as counter and reference electrodes, respectively, for all electrochemical measurements.

2.4. Photocatalytic tests

Photocatalytic CO_2 reduction tests were carried out in a closed quartz reactor (55 ml volume). First, 20 mg of the catalyst were dispersed in 4 ml of water under vigorous stirring. Then, 4 ml of triethanolamine (TEOA) and 12 ml of acetonitrile were added to have a final solvent composition of CH_3CN:H_2O:TEOA = 3:1:1 in volume. The dispersion was sonicated for 15 min and then 6.6 mg of $Ru(bpy)_3Cl_2{\cdot}6H_2O$ were dissolved in this suspension. After 15 min of stirring, the orange dispersion was transferred to the photoreactor and pure CO_2 was bubbled into the mixture for 10 min, filling the reactor with a final overpressure of 0.5 bar. The temperature of the reactor was controlled at 40 °C during the test.

The activity of each catalyst was tested upon irradiation with a Newport Oriel® Sol1A™ Class ABB 94041A solar simulator equipped with a Xe arc lamp and a AM 1.5G filter. The course of the photoreaction was followed by analysing aliquots from the head space at fixed intervals. Hydrogen evolved was analysed using a gas chromatograph (Agilent 490 MicroGC) equipped with a Mol Sieve 5 Å column and a TCD detector using Ar as the carrier gas. CO and CH_4 produced in the irradiation were determined using a gas chromatograph (Agilent 7890 A GC System) equipped with a Carboxen®-1010 PLOT Capillary GC Column with a TCD detector using He as the carrier gas.

For the recyclability tests, the materials were collected after reaction by centrifugation (12,000 rpm, 15 min) and washed twice with water. Afterwards, the solid was dispersed in 20 ml of a CH_3CN:H_2O:TEOA 3:1:1 in volume mixture. Finally, 6.6 mg of $Ru(bpy)_3Cl_2{\cdot}6H_2O$ were dissolved in the suspension. The successive tests were carried out as described above.

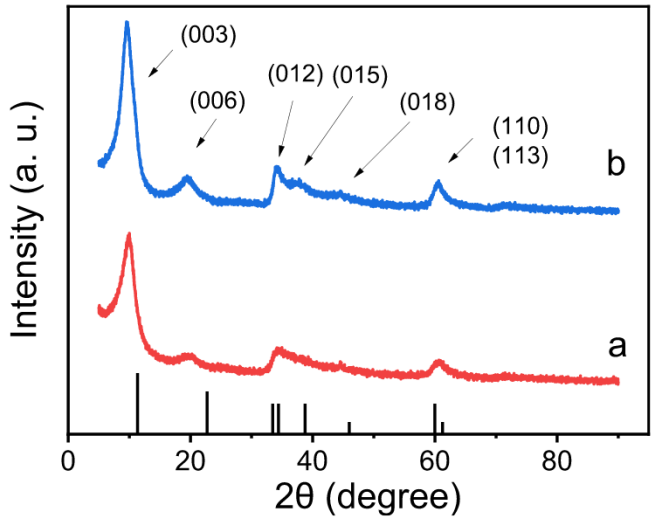

Fig. 1. PXRD patterns of NiTiAl (a) and NiAl (b) LDHs.

3. Results and discussion

3.1. Material characterisation

Three LDHs were prepared in the present study. One of them is a trimetallic NiTiAl-LDH synthesised by solvothermal method using methanol as solvent and urea as alkalizing agent. Bimetallic NiAl-LDH was also synthesised following the same procedure, but in absence of Ti precursor. Finally, trimetallic NiTiAl-bulk was synthesised by traditional hydrothermal method to compare the effect of the morphology over the catalytic activity. In this study, a Ti complex that is stable in aqueous solution was employed as the Ti source, facilitating the incorporation of this metal to the structure, since competitive processes of TiO_2 formation were avoided.

XRD patterns of both NiAl and NiTiAl LDH materials (Fig. 1, S1) show the typical reflections of the α-$Ni(OH)_2$ structure (JCPDS card No. 38-0715). The peaks at 2θ values of 10 and 20 degrees are related with the (*0, 0, l*) faces of the material and the *c* parameter of the unit cell. The basal space is the distance between two consecutive layers and its value is 1/3 of the *c* parameter. The basal space obtained for NiTiAl material is 8.8 Å, which corresponds to a LDH structure having intercalated nitrate anions [13]. The value obtained for NiAl is 9.3 Å, associated with methoxy anions intercalation [35,36]. The peak around 60° is related with the *a* parameter of the unit cell. Values of cell parameters for both structures are given in Table 1. The cation composition of the LDH samples was determined by EDX, being 3:0.5:0.8 for NiTiAl-LDH and 2.5:1 for NiAl-LDH (Table 1, S1).

FESEM images of the samples (Fig. 2) reveal the influence of the composition on the particle morphology under the same synthesis conditions. NiTiAl-LDH sample shows a morphology composed of crosslinked nanosheets that assemble in nanoball superstructures with a diameter in the range 100–600 nm as seen in Fig. 2a-b. On the other hand, NiAl-LDH nanosheets present larger lateral size and thickness, and the nanoball superstructure is in general less regular (Fig. 2c-d). The particle size is larger (several micrometres) compared to the nanoballs present in NiTiAl-LDH, which agrees with the higher degree of crystallinity found for NiAl in the XRD pattern. FESEM image of NiTiAl-bulk LDH (Fig. S2a) shows higher degree of aggregation.

Table 1
Cation composition, BET surface area and cell parameters from XRD data for NiTiAl and NiAl LDHs.

	Material	
	NiTiAl-LDH	NiAl-LDH
a (Å)	3.0	3.0
c (Å)	26.4	27.9
BS[a] (Å)	8.8	9.3
%Ni	69.6	71.4
%Al	12.0	28.6
%Ti	18.4	0.0
Theor. Ratio	4:0.5:0.5	4:1
Exp. Ratio	3:0.5:0.8	2.5:1
BET Area (m^2/g)	3.25	0.44

[a] BS: basal spacing.

To further study the particle size difference between both materials, DLS analysis of the samples suspended in ethanol was carried out (Fig. 3). The larger average particle size in NiAl-LDH (500–1200 nm) compared to NiTiAl-LDH (100–500 nm) was also observed for the suspended nanosheets.

TEM images of the samples further confirm the difference in particle size and morphology between both materials. NiTiAl-LDH TEM image (Fig. 4a) shows a nanosheet thickness of 2–4 nm, implying the stacking of very few layers of the material, providing higher number of accessible active sites. On the other hand, NiAl-LDH (Fig. 4b) presents a more aggregated morphology typical of hydrotalcites prepared by alcohothermal synthesis [37], with a nanosheet thickness of 15–20 nm. Larger particle size of NiTiAl-bulk LDH is also confirmed by TEM (Fig. S2b).

3.2. Photocatalytic activity

The photocatalytic activity for CO_2PR for the NiTiAl-LDH, NiAl-LDH, NiTiAl-Bulk LDH and a blank in the absence of any catalyst but in the presence of $Ru(bpy)_3Cl_2$ and TEOA is presented in Fig. 5. No catalytic activity was observed in absence of TEOA or $Ru(bpy)_3Cl_2$. For the NiTiAl-LDH the main product is methane (148 μmol g^{-1} h^{-1}) with a selectivity of 86%. This value represents, to the best of our knowledge, the highest selectivity towards methane reported for LDH materials in similar conditions (Table S2). In the case of NiAl-LDH, the main product is CO, with no methane production. The amount of CO evolved is 328 μmol g^{-1} h^{-1}. Some hydrogen is also produced, at a rate of 74 μmol g^{-1} h^{-1}. The products evolved by the blank sample come from the activity of the $Ru(bpy)_3Cl_2$ complex, (49 μmol g^{-1} h^{-1} H_2, 34 μmol g^{-1} h^{-1} CO) that exhibits some activity in the conditions of the photocatalytic reaction [28]. The amounts of evolved products were normalised to the number of equivalent electrons consumed assuming that 2 electrons are needed for H_2 or CO evolution and 8 electrons for the reduction to CH_4. The normalised production obtained was 1229 μmol e^- g^{-1} h^{-1} for NiTiAl-LDH, 803 μmol e^- g^{-1} h^{-1} for NiAl-LDH and 167 μmol e^- g^{-1} h^{-1} for the control sample with $Ru(bpy)_3^{2+}$. Thus, NiTiAl-LDH is also more efficient than the bimetallic NiAl-LDH or $Ru(bpy)_3^{2+}$.

The competition of HER is decreased when a LDH catalyst is used probably due to the favourable adsorption of CO_2 on LDH nanosheets. Thus, selectivity towards hydrogen production is 59.1% for the control using $Ru(bpy)_3Cl_2$ and TEOA, but it becomes 18.3% for NiAl-LDH and it is almost suppressed by NiTiAl-LDH (only 5.8% selectivity).

To prove the stability of the materials, recyclability tests were carried out. As it is shown in Fig. S3, the amount and distribution of products evolved remain stable for NiTiAl-LDH catalyst over three different catalytic cycles. The small decrease of production in every consecutive cycle can be explained as an effect of the loss of catalyst mass over the different recovery processes. The stability of the material was confirmed by XRD and EDX analysis of the recovered sample (Fig. S4, Table S3).

From the different product selectivity, it can be inferred that the mechanism through which the reaction is carried out is different for each one of the samples. In the case of the homogeneous photocatalytic process, in which the $Ru(bpy)_3Cl_2$ is the active species, the

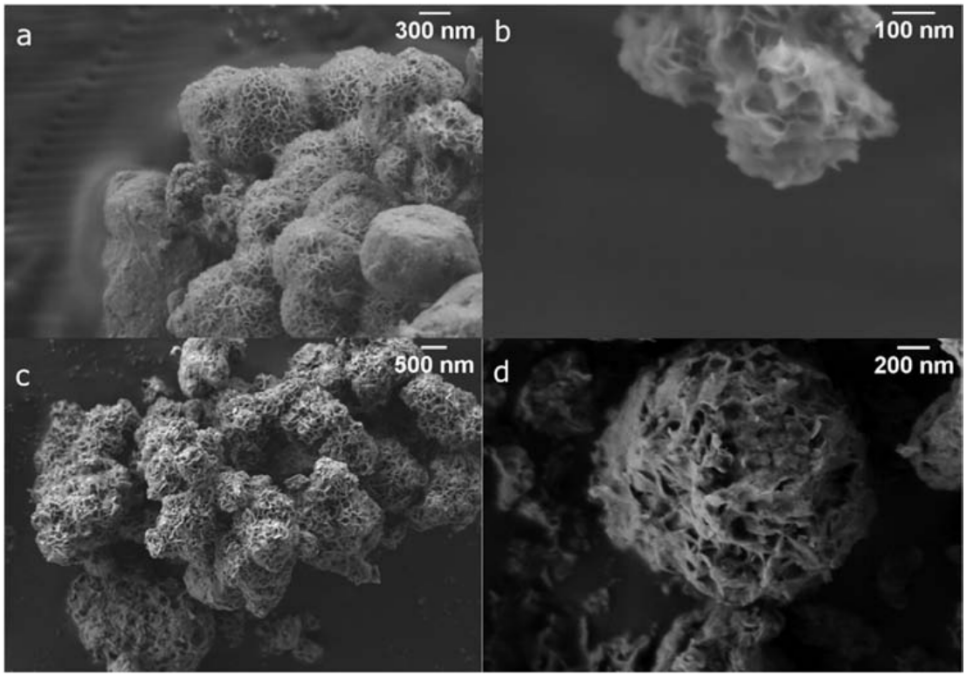

Fig. 2. FESEM images of NiTiAl-LDH (a, b) and NiAl-LDH (c, d).

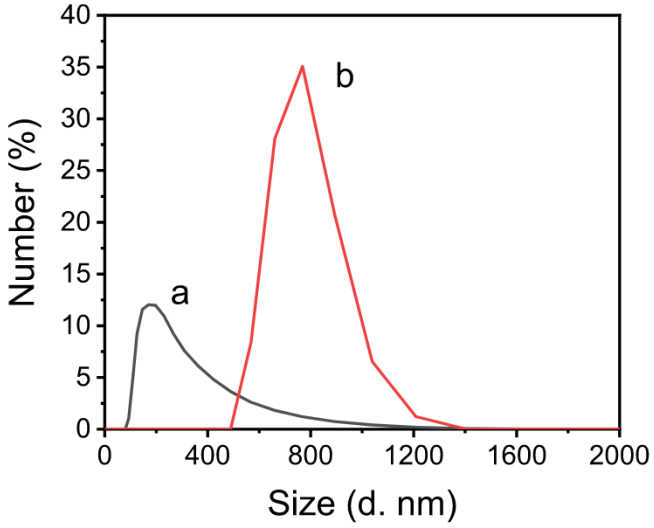

Fig. 3. Particle size distribution of NiTiAl (a) and NiAl (b) LDHs suspensions in ethanol ($7.5{\cdot}10^{-2}$ g/L) by DLS analysis.

presence of H_2O in its solvation sphere probably favours H_2 evolution. When the LDH catalyst is introduced, an electron transfer from $Ru(bpy)_3^{2+}$ in its triplet excited state to LDH would take place. The favourable CO_2 adsorption on LDH increases selectivity towards CO_2 reduction products, respect to H_2O. CO_2 adsorption on LDHs occurs on the surface hydroxyl groups present in the LDH (basic sites) that have affinity for the acidic CO_2 molecule[19].

To explain the contrasting photocatalytic behaviour of the synthetised materials, diffuse reflectance UV–visible spectroscopy measurements were performed. As seen in Fig. 6a, NiAl-LDH presents three main absorption bands: the first one in the range of 200–300 nm, the second at 300–500 nm, and the third one at 600–800 nm. The first one can be attributed to the ligand-to-metal charge transfer (LMCT) from the O 2p orbital to the Ni 3d t_{2g} orbital, while the other two correspond to characteristic d-d transition of the Ni(II) cation in octahedral geometry [38]. In the NiTiAl-LDH material, the first band is shifted to higher wavelengths, due to the contribution of titanium [39], and the first Ni(II) d-d band is merged with it. The other Ni(II) band at 600–800 nm is like the one present in NiAl-LDH.

The band gap of the materials can be determined using the Tauc Equation:

$$\alpha h\upsilon = K(h\upsilon - E_g)^n \quad (1)$$

where α, h, ν, K and E_g are the absorption coefficient, Planck constant, light frequency, proportionality constant and the optical band gap of the material, respectively. The value of n parameter is related to the electronic transition in a semiconductor. Its possible values are 1/2, 3/2, 2 and 3 for direct allowed, direct forbidden, indirect allowed and indirect forbidden transitions, respectively [40]. For the materials under study, the band gap value was calculated from the $(F(R)h\nu)^{1/n}$ vs. hν plot, where F(R) is Kubelka-Munk function, proportional to the absorption coefficient. A value of $n = 2$ was chosen for the calculations, corresponding with an indirect allowed transition as reported in the literature for these materials [28,41,42]. The calculated band gaps were 3.16 eV for NiTiAl-LDH and 4.41 eV for NiAl-LDH (Fig. 6b). These band gap values correspond to UV absorptions. Thus, under the present experimental conditions $Ru(bpy)_3^{2+}$ dye should be the light harvester.

It can be observed that the presence of titanium in the composition of the LDH structure also has an important role in the reaction mechanism, since it changes completely the main product of the CO_2PR from CO in its absence to CH_4 when Ti is incorporated within the layers. CO evolution is the most frequently observed process in the CO_2PR using LDH [3,19]. In contrast, in the present study, it was observed that the presence of Ti in the composition drives the selectivity towards CH_4.

To demonstrate the effect of Ti in the electronic structure of the material, XPS studies were performed. From Ni 2p XPS spectra of NiTiAl and NiAl samples (Fig. S6a), a shift of the peaks to higher binding energies for the Ti-containing material proves the electronic interaction between Ni(II) and Ti(IV) cations, resulting into a lower electron density over Ni(II) centres.

In addition, valence band XPS experiments (Fig. S6b) were carried out to determine the position of the valence band edges for

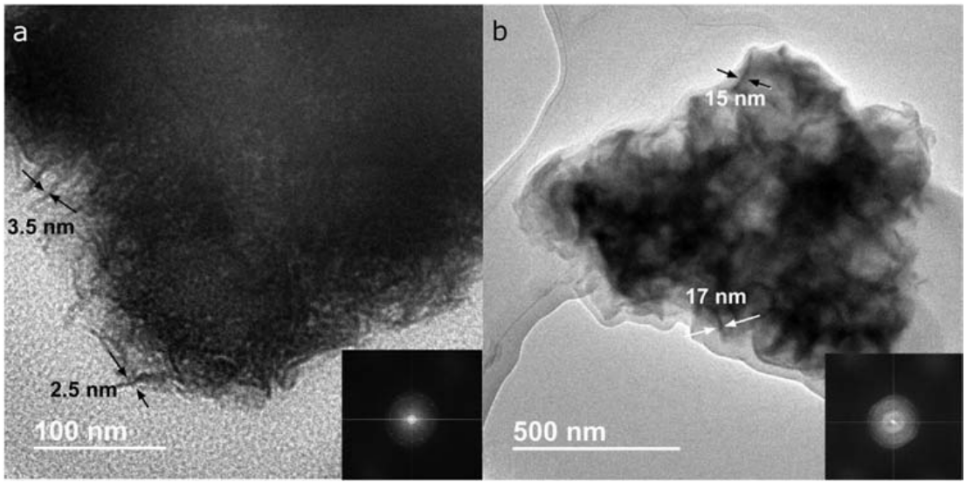

Fig. 4. TEM images and SAED patterns (inserts) of NiTiAl (a) and NiAl (b) LDHs.

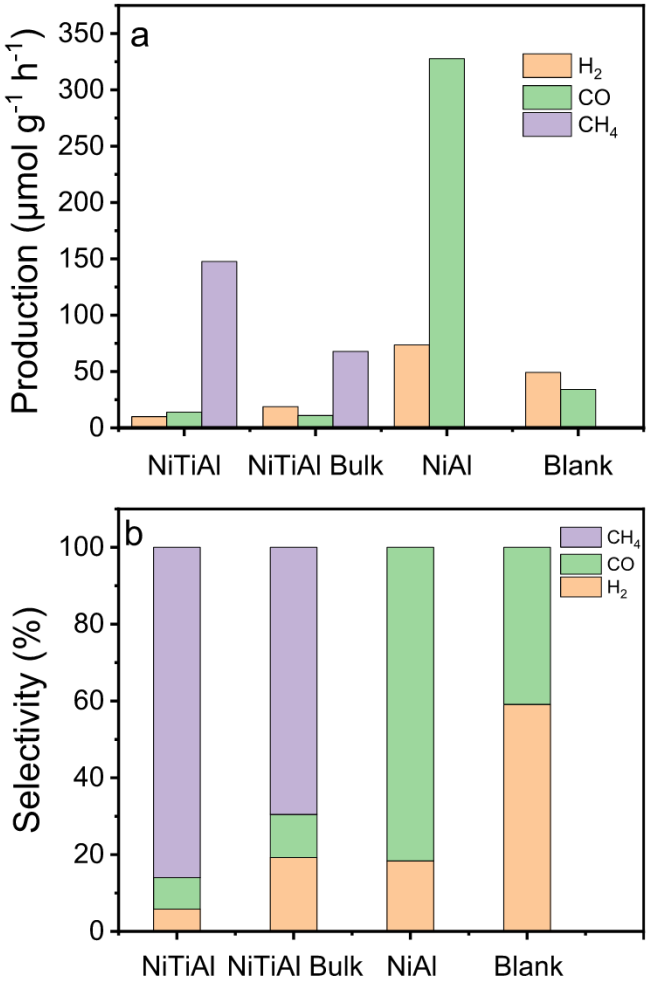

Fig. 5. Production (a) and selectivity (b) obtained in the photocatalytic CO_2 reduction reaction conditions.

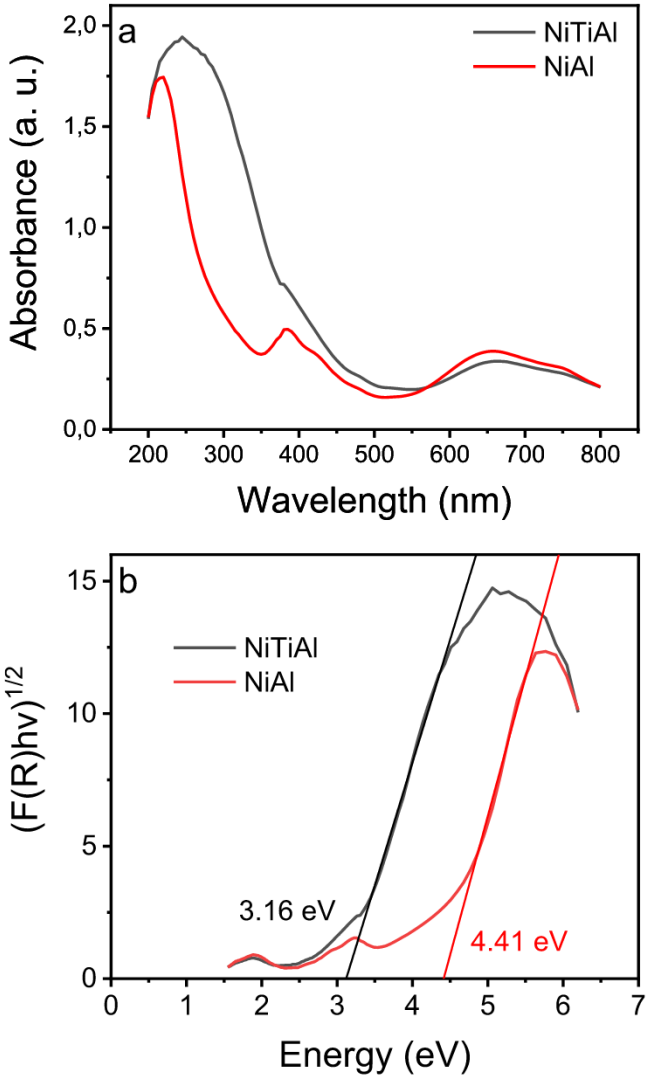

Fig. 6. UV–Vis diffuse reflectance spectra (a) and Tauc plots (b) of the samples.

NiTiAl and NiAl LDHs, which were 2.79 V and 0.4 V vs NHE respectively. The position of the conduction band edges could be calculated using band gap values obtained from Tauc plots, resulting in − 0.37 V and − 4.01 V vs NHE.

The potential of the conduction band of NiTiAl-LDH was higher than the redox potential of the CO_2/CH_4 pair, but lower than CO_2/CO couple, which explained the change in selectivity after the introduction of Ti in the structure. In a hypothetical mechanism, when the $Ru(bpy)_3^{2+}$ absorbs visible light photons, electrons are promoted from HOMO to LUMO. Those electrons are transferred to

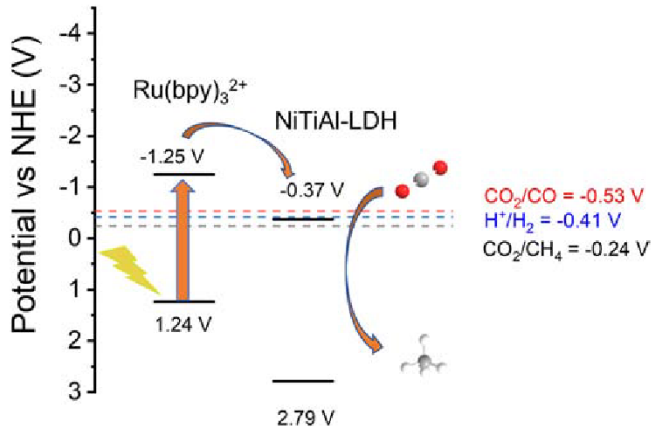

Scheme 1. Band structure of NiTiAl-LDH and probable photocatalytic mechanism for CO_2 reduction to methane. Energy levels of $Ru(bpy)_3^{2+}$ versus vacuum level have been confirmed as 5.68 V for HOMO and 3.19 V for LUMO [4]. Data processing for obtained values vs NHE can be found in Fig. S6b.

NiTiAl-LDH, and then to the adsorbed CO_2 molecules, that are reduced to methane (Scheme 1).

To support the CH_4 selectivity in the case of NiTiAl-LDH, CO adsorption measurements were performed. It was observed that CO adsorption on NiTiAl-LDH is higher than on NiAl-LDH (Fig. S7). Based on this data, it is proposed that CO, which is preferably produced by NiAl-LDH, evolved to the gas phase once formed in the case of NiAl-LDH photocatalyst. In contrast, CO as reaction intermediate would remain strongly adsorbed in NiTiAl-LDH and, therefore, will react further resulting in the formation of the most reduced CH_4 product. BET surface area analysis of the materials was also carried out (Table 1, S1). The values obtained were 3,25 m^2/g for NiTiAl-LDH, 0,44 m^2/g for NiAl-LDH and 97,99 m^2/g for NiTiAl-Bulk LDH. It can be observed that there is no direct correlation between the surface area and the activity of the material.

From the EIS analysis of the samples (Fig. S8) a lower arc radius was observed for Ti-containing samples, which revealed that those systems had lower charge transfer resistance.

Photocurrent measurements were carried out to complement the understanding of the photocatalytic behaviour of the materials (Fig. 7). Under the same irradiation conditions using thin film of LDH deposited on FTO as working electrode, the obtained photocurrent values were around 600 nA for NiTiAl-LDH and 900 nA for NiAl-LDH. These values were obtained while irradiating with a full spectrum Xe lamp, switching on and off the lamp every 10 s. If a 380 nm filter (cutting all the wavelengths shorter than 380 nm) is used, no appreciable photocurrent is observed for any of the two LDHs. That means that the charge separation on the LDH present in this study only takes place under UV light irradiation. This implies that the band corresponding to ligand-to-metal charge transfer observed in the absorption spectrum in the range of 200–400 nm is the responsible of the photoresponse, while the Ni d-d electronic transitions do not contribute to charge separation, in accordance with the calculated band gap. Photocurrent measurements explain why there is no catalytic activity in absence of Ru complex. This proves that in the photocatalytic tests carried out in this work, $Ru(bpy)_3^{2+}$ is responsible of the light absorption, since the material was irradiated with simulated solar light and LDH only absorbs UV-light photons, which is a very small portion of solar light.

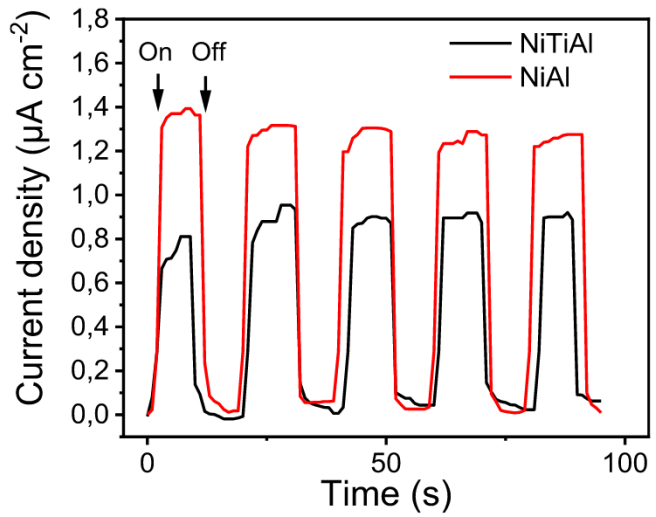

Fig. 7. Photocurrent measurements of NiAl and NiTiAl LDHs by turning on and off the illumination at regular time intervals. Electrolyte: 0.1 M $LiClO_4$ aq. (5% vol. methanol). Electrochemical cell: LDH/FTO working electrode, Ag/AgCl reference electrode and Pt counter electrode. Atmosphere: N_2. Light source: 300 W Xe lamp.

The particle morphology has also a big impact in the photoactivity. Due to its smaller sheet dimension and thickness, there is a higher degree of exposure of the active sites for NiTiAl-LDH compared to NiTiAl-bulk, which increases CH_4 production.

4. Conclusions

A new trimetallic LDH material containing Ni, Ti and Al cations has been synthetised by alcohothermal method. The incorporation of titanium results in a nanoball morphology, with a smaller particle size for the trimetallic NiTiAl-LDH than the NiAl-LDH samples. When applied on the CO_2 photoreduction reaction, the catalyst yields 86% selectivity towards methane production, almost suppressing the H_2 or CO evolution under solar light. This selectivity has been attributed to the band structure of the Ti-containing material, whose band edges placement are more suitable for CO_2 reduction to CH_4 than CO. The electronic interaction between Ni(II) and Ti(IV) produces a shift on the band edges position and reduces the optical band gap of the material. A probable reduction mechanism was proposed in which $Ru(bpy)_3^{2+}$ would absorb visible light photons and transfer electrons to the conduction band of NiTiAl-LDH at a lower potential than the redox potential of the CO_2/CO couple. Thus, NiTiAl-LDH would transfer the electrons to CO_2 reducing it to CH_4 instead. This work features the high tuneability of LDH materials to drive product selectivity, and how the understanding of the structure-function relationship can lead to the pre-design of the material according to the target reaction.

CRediT authorship contribution statement

Manuel Molina-Muriel: Investigation, Data curation, Writing – original draft. **Yong Peng:** Investigation, Data curation. **Hermenegildo García:** Writing – review & editing, Supervision. **Antonio Ribera:** Writing – review & editing, Supervision.

Declaration of Competing Interest

The authors declare that they have no known competing financial interests or personal relationships that could have appeared to influence the work reported in this paper.

Acknowledgments

We thank the grant CTQ2017-87201-P, Severo Ochoa and RTI2018.98237-B-CO1 funded by MCIN/AEI/10.13039/501100011033 and by "ERDF A way of making Europe" for financial support. Generalitat Valenciana (Prometeo 2017/083 and Prometeo 2019/076)

is also gratefully acknowledged. M.M. thanks the Universitat Politecnica de Valencia for a postgraduate scholarship.

Appendix A. Supporting information

Supplementary data associated with this article can be found in the online version at doi:10.1016/j.jallcom.2021.163124.

References

[1] X. Li, J. Yu, M. Jaroniec, X. Chen, Cocatalysts for selective photoreduction of CO_2 into solar fuels, Chem. Rev. 119 (2019) 3962–4179.

[2] Y. Yang, J. Wu, T. Xiao, Z. Tang, J. Shen, H. Li, Y. Zhou, Z. Zou, Urchin-like hierarchical CoZnAl-LDH/RGO/g-C_3N_4 hybrid as a Z-scheme photocatalyst for efficient and selective CO_2 reduction, Appl. Catal. B 255 (2019) 117771.

[3] L. Tan, Z. Wang, Y. Zhao, Y. Song, Recent progress on nanostructured layered double hydroxides for visible-light-induced photoreduction of CO_2, Chem. - Asian J. 15 (2020) 3380–3389.

[4] K.Q. Lu, Y.H. Li, F. Zhang, M.Y. Qi, X. Chen, Z.R. Tang, Y. Yamada, M. Anpo, M. Conte, Y.J. Xu, Rationally designed transition metal hydroxide nanosheet arrays on graphene for artificial CO_2 reduction, Nat. Commun. 11 (2020) 5181.

[5] H. Zhang, Y. Wang, S. Zuo, W. Zhou, J. Zhang, X.W.D. Lou, Isolated cobalt centers on $W_{18}O_{49}$ nanowires perform as a reaction switch for efficient CO_2 photoreduction, J. Am. Chem. Soc. 143 (2021) 2173–2177.

[6] X. Jiao, K. Zheng, L. Liang, X. Li, Y. Sun, Y. Xie, Fundamentals and challenges of ultrathin 2D photocatalysts in boosting CO_2 photoreduction, Chem. Soc. Rev. 49 (2020) 6592–6604.

[7] C.S. Diercks, Y. Liu, K.E. Cordova, O.M. Yaghi, The role of reticular chemistry in the design of CO_2 reduction catalysts, Nat. Mater. 17 (2018) 301–307.

[8] M.J. Wu, J.Z. Wu, J. Zhang, H. Chen, J.Z. Zhou, G.R. Qian, Z.P. Xu, Z. Du, Q.L. Rao, A review on fabricating heterostructures from layered double hydroxides for enhanced photocatalytic activities, Catal. Sci. Technol. 8 (2018) 1207–1228.

[9] Y. Zhao, X. Jia, G.I.N. Waterhouse, L.Z. Wu, C.H. Tung, D. O'Hare, T. Zhang, Layered double hydroxide nanostructured photocatalysts for renewable energy production, Adv. Energy Mater. 6 (2016) 1501974(n/a).

[10] G. Zhao, J. Zou, X. Chen, J. Yu, F. Jiao, Layered double hydroxides materials for photo(electro-) catalytic applications, Chem. Eng. J. 397 (2020) 125407.

[11] S. Ng, M.Y.L. Lau, W. Ong, Engineering layered double hydroxide–based photocatalysts toward artificial photosynthesis: state-of-the-art progress and prospects, Sol. Rrl. 5 (2021) 2000535.

[12] X. Bian, S. Zhang, Y. Zhao, R. Shi, T. Zhang, Layered double hydroxide-based photocatalytic materials toward renewable solar fuels production, InfoMat 3 (2021) 719–738.

[13] F. Cavani, F. Trifiro, A. Vaccari, Hydrotalcite-type anionic clays: preparation, properties and applications, Catal. Today 11 (1991) 173–301.

[14] N. Vu, S. Kaliaguine, T. Do, Critical aspects and recent advances in structural engineering of photocatalysts for sunlight-driven photocatalytic reduction of CO_2 into fuels, Adv. Funct. Mater. 29 (2019) 1901825(n/a).

[15] Y. Zhao, G. Chen, T. Bian, C. Zhou, G.I. Waterhouse, L.Z. Wu, C.H. Tung, L.J. Smith, D. O'Hare, T. Zhang, Defect-rich ultrathin ZnAl-layered double hydroxide nanosheets for efficient photoreduction of CO_2 to CO with water, Adv. Mater. 27 (2015) 7824–7831.

[16] R. Wang, Z. Qiu, S. Wan, Y. Wang, Q. Liu, J. Ding, Q. Zhong, Insight into mechanism of divalent metal cations with different d-bands classification in layered double hydroxides for light-driven CO_2 reduction, Chem. Eng. J. 427 (2022) 130863.

[17] Y. Su, Z. Song, W. Zhu, Q. Mu, X. Yuan, Y. Lian, H. Cheng, Z. Deng, M. Chen, W. Yin, Y. Peng, Visible-light photocatalytic CO_2 reduction using metal-organic framework derived $Ni(OH)_2$ nanocages: a synergy from multiple light reflection, static charge transfer, and oxygen vacancies, ACS Catal. 11 (2021) 345–354.

[18] Z. Li, Z. Liu, Y. Li, Q. Wang, Flower-like CoAl layered double hydroxides modified with CeO_2 and RGO as efficient photocatalyst towards CO_2 reduction, J. Alloy. Compd. 881 (2021) 160650.

[19] Z. Yang, J. Wei, G. Zeng, H. Zhang, X. Tan, C. Ma, Xc Li, Zh Li, C. Zhang, A review on strategies to LDH-based materials to improve adsorption capacity and photoreduction efficiency for CO_2, Coord. Chem. Rev. 386 (2019) 154–182.

[20] K. Bhattacharyya, G.P. Mane, V. Rane, A.K. Tripathi, A.K. Tyagi, Selective CO_2 photoreduction with Cu-Doped TiO_2 photocatalyst: delineating the crucial role of Cu-oxidation state and oxygen vacancies, J. Phys. Chem. C 125 (2021) 1793–1810.

[21] C. Chen, J. Jin, S. Chen, T. Wang, J. Xiao, T. Peng, In-situ growth of ultrafine ZnO on g-C_3N_4 layer for highly active and selective CO_2 photoreduction to CH4 under visible light, Mater. Res. Bull. 137 (2021) 111177.

[22] Y. Gao, L. Zhang, Y. Gu, W. Zhang, Y. Pan, W. Fang, J. Ma, Y.Q. Lan, J. Bai, Formation of a mixed-valence Cu(I)/Cu(II) metal-organic framework with the full light spectrum and high selectivity of CO_2 photoreduction into CH_4, Chem. Sci. 11 (2020) 10143–10148.

[23] J. An, T. Shen, W. Chang, Y. Zhao, B. Qi, Y. Song, Defect engineering of NiCo-layered double hydroxide hollow nanocages for highly selective photoreduction of CO_2 to CH_4 with suppressing H_2 evolution, Inorg. Chem. Front. 8 (2021) 996–1004.

[24] D. Adekoya, M. Tahir, N.A.S. Amin, Recent trends in photocatalytic materials for reduction of carbon dioxide to methanol, Renew. Sustain. Energy Rev. 116 (2019) 109389.

[25] K. Niu, Y. Xu, H. Wang, R. Ye, H.L. Xin, F. Lin, C. Tian, Y. Lum, K.C. Bustillo, M.M. Doeff, M. Koper, J. Ager, R. Xu, H. Zheng, A spongy nickel-organic CO_2 reduction photocatalyst for nearly 100% selective CO production, Sci. Adv. 3 (2017) e1700921.

[26] J. Wang, T. Xia, L. Wang, X. Zheng, Z. Qi, C. Gao, J. Zhu, Z. Li, H. Xu, Y. Xiong, Enabling visible-light-driven selective CO_2 reduction by doping quantum dots: trapping electrons and suppressing H_2 evolution, Angew. Chem. Int. Ed. 57 (2018) 16447–16451.

[27] F. Sastre, A. Corma, H. Garcia, Visible-light photocatalytic conversion of carbon monoxide to methane by nickel(II) oxide, Angew. Chem. Int. Ed. 52 (2013) 12983–12987.

[28] L. Tan, S.M. Xu, Z. Wang, Y. Xu, X. Wang, X. Hao, S. Bai, C. Ning, Y. Wang, W. Zhang, Y.K. Jo, S. Hwang, X. Cao, X. Zheng, H. Yan, Y. Zhao, H. Duan, Y. Song, Highly selective photoreduction of CO_2 with suppressing H_2 evolution over monolayer layered double hydroxide under irradiation above 600 nm, Angew. Chem. Int. Ed. 58 (2019) 11860–11867.

[29] Z. Wang, A. Hao, P. Xing, Engineering active Ni sites in ternary layered double hydroxide nanosheets for a highly selective photoreduction of CO_2 to CH_4 under irradiation above 500 nm, Ind. Eng. Chem. Res. 59 (2020) 3008–3015.

[30] Z. Wang, S.M. Xu, L. Tan, G. Liu, T. Shen, C. Yu, H. Wang, Y. Tao, X. Cao, Y. Zhao, Y.F. Song, 600 nm-driven photoreduction of CO_2 through the topological transformation of layered double hydroxides nanosheets, Appl. Catal. B 270 (2020) 118884.

[31] L. Tan, S. Xu, Z. Wang, X. Hao, T. Li, H. Yan, et al., 600 nm induced nearly 99% selectivity of CH_4 from CO_2 photoreduction using defect-rich monolayer structures, Cell Rep. Phys. Sci. 2 (2021) 100322.

[32] S. Bai, T. Li, H. Wang, L. Tan, Y. Zhao, Y. Song, Scale-up synthesis of monolayer layered double hydroxide nanosheets via separate nucleation and aging steps method for efficient CO_2 photoreduction, Chem. Eng. J. 419 (2021) 129390.

[33] X. Xiong, Y. Zhao, R. Shi, W. Yin, Y. Zhao, G.I.N. Waterhouse, T. Zhang, Selective photocatalytic CO_2 reduction over Zn-based layered double hydroxides containing tri or tetravalent metals, Sci. Bull. 65 (2020) 987–994.

[34] C. Lin, N. Xia, S. Zhou, J. Tian, H. Li, Surfactant-free approach for engineering an ultrathin Ti-Doped $Ni(OH)_2$ nanosheet on carbon cloth: experimental and theoretical insight into boosted alkaline water oxidation activity, Inorg. Chem. 59 (2020) 10253–10261.

[35] J.A. Carrasco, J. Romero, M. Varela, F. Haukec, G. Abellan, A. Hirsch, et al., Alkoxide-intercalated NiFe-layered double hydroxides magnetic nanosheets as efficient water oxidation electrocatalysts, arXiv. Org. e-Print. Arch., Phys. (2018) 1–29.

[36] E. Gardner, K.M. Huntoon, T.J. Pinnavaia, Direct synthesis of alkoxide-intercalated derivatives of hydrotalcite-like layered double hydroxides: precursors for the formation of colloidal layered double hydroxide suspensions and transparent thin films, Adv. Mater. 13 (2001) 1263–1266.

[37] Z. Lu, L. Qian, W. Xu, Y. Tian, M. Jiang, Y. Li, X. Sun, X. Duan, Dehydrated layered double hydroxides: alcohothermal synthesis and oxygen evolution activity, Nano Res. 9 (2016) 3152–3161.

[38] S. Tonda, S. Kumar, M. Bhardwaj, P. Yadav, S. Ogale, g-C_3N_4/NiAl-LDH 2D/2D hybrid heterojunction for high-performance photocatalytic reduction of CO_2 into renewable fuels, ACS Appl. Mater. Interfaces 10 (2018) 2667–2678.

[39] Y. Zhao, B. Li, Q. Wang, W. Gao, C.J. Wang, M. Wei, D.G. Evans, X. Duan, D. O'Hare, NiTi-Layered double hydroxides nanosheets as efficient photocatalysts for oxygen evolution from water using visible light, Chem. Sci. 5 (2014) 951–958.

[40] R. Lopez, R. Gomez, Band-gap energy estimation from diffuse reflectance measurements on sol-gel and commercial TiO_2: a comparative study, J. Sol-Gel Sci. Technol. 61 (2012) 1–7.

[41] S. Xu, H. Yan, M. Wei, Band structure engineering of transition-metal-based layered double hydroxides toward photocatalytic oxygen evolution from water: a theoretical–experimental combination study, J. Phys. Chem. C 121 (2017) 2683–2695.

[42] S. Bai, Z. Wang, L. Tan, G.I.N. Waterhouse, Y. Zhao, Y. Song, 600 nm irradiation-induced efficient photocatalytic CO_2 reduction by ultrathin layered double hydroxide nanosheets, Ind. Eng. Chem. Res 59 (2020) 5848–5857.